Nanoelectromechanical devices in a fluidic environment

Oleksiy Svitelskiy*
Department of Physics, University of Alberta, Edmonton, Alberta, Canada T6G 2G7 and
National Institute for Nanotechnology, Edmonton, Alberta, Canada T6G 2M9

Vince Sauer
National Institute for Nanotechnology, Edmonton, Alberta, Canada T6G 2M9 and
Department of Electrical and Computer Engineering, University of Alberta, Edmonton, Alberta, Canada T6G 2V4

Douglass Vick and Kar-Mun Cheng
National Institute for Nanotechnology, Edmonton, Alberta, Canada T6G 2M9

Ning Liu
Department of Physics, University of Alberta, Edmonton, Alberta, Canada T6G 2G7

Mark R. Freeman and Wayne K. Hiebert
National Institute for Nanotechnology, Edmonton, Alberta, Canada T6G 2M9 and
Department of Physics, University of Alberta, Edmonton, Alberta, Canada T6G 2G7
(Received 16 January 2012; published 29 May 2012; corrected 1 June 2012)

We present a comprehensive study of nanoelectromechanical systems in pressurized fluids. Resonant responses and quality factors are monitored in five different gases and one liquid, in pressures ranging from vacuum to 20 MPa, in order to evaluate theoretical models of device-fluid interactions at the nanoscale. The traditional Newell picture of microresonator damping in different pressure regimes is found to be inadequate in describing nanoresonators in general. Damping at intermediate pressure ranges is better physically characterized by a Weissenberg number (which compares oscillation frequencies with fluid relaxation rates) than a Knudsen number (which compares mean free paths with device widths) and most adequately described by the Yakhot and Colosqui model. At high-pressure ranges, two models are found to give good agreement with data: the phenomenological model of vibrating spheres and the Sader and Bhiladvala model for the viscous regime. The latter is also successful in explicitly predicting pressure-dependent behavior of the viscous mass load and damping. We observe significant increases in damping due to the squeezed film (SF) of gas between the device and substrate as well as due to undercut (an unavoidable artifact of the standard fabrication technique); correcting the shape of the devices with a focused ion beam allows us to differentiate these two factors. Application of the SF model accounts well for additional damping at high pressures while only qualitatively agreeing at lower pressures. The extensive data collected allow additional insight into fundamental processes underlying fluid damping at the nanoscale, particularly in the intermediate- and high-pressure regimes.

DOI: 10.1103/PhysRevE.85.056313 PACS number(s): 47.61.Fg, 85.85.+j, 47.50.Ef, 62.25.Jk

I. INTRODUCTION

Nanoelectromechanical systems (NEMSs) are promising candidates for a wide variety of applications [1–8], many of which require operation in gas and liquid environments [9–13]. The emerging importance of nanoscale fluid dynamics to nanoscience is also becoming clear [14–24]. Understanding the full picture of device-fluid interactions and damping at the nanoscale requires working over a very broad and technically challenging pressure range [24]. In this paper, we explore the full suite of theoretical models that address fluidic dissipation, garnering insight into not only their applicability but also the validity of their theoretical underpinnings.

Two alternative theoretical approaches attempt to describe NEMS behavior in the damping environment of fluid. One characterizes the pressure regime in terms of the Knudsen number, as suggested by Newell [14] and developed in the Sader [15] and Bhiladvala and Wang [16] theory (SBT) $\mathrm{Kn} \approx \lambda_{\mathrm{mfp}}/w$, where λ_{mfp} is the mean free path of the gas molecules and w is the characteristic size (width) of the device. The other describes pressure-device regimes in terms of the Weissenberg number, as suggested by Yakhot and Colosqui theory [17] (YCT) $\mathrm{Wi} \approx \omega\tau$, where ω is the NEMS angular frequency and τ is a fluid relaxation time. With both, three essentially different pressure regimes can be defined: a low-pressure regime $\mathrm{Kn} > 1$ and $\mathrm{Wi} > 1$; an intermediate-pressure regime $\mathrm{Kn} \sim 1$ and $\mathrm{Wi} \sim 1$; and a high-pressure regime $\mathrm{Kn} < 1$ and $\mathrm{Wi} < 1$. Accounting for the effects of the squeezed film (SF) of fluid between the device and substrate represents an additional problem.

So far, the actual performance of a NEMS has been exhaustively tested for a few limiting cases only. While it was shown to be possible to approximate vibrations of very thin long beams by Sader's approach [18,19], the task

*Present address: Department of Physics and Astronomy, Colgate University, Hamilton, NY 13346; oleksiysvit@yahoo.com

 ©2012 American Physical Society

of developing an adequate description for the case of real beams of rectangular shape is more complicated. Several works done below and slightly above atmospheric pressure (up to 0.13 MPa), fully covering only the first operating regime and, partially, the second, proved the acceptable applicability of the free molecular flow (FMF) approximation for the low-pressure regime [20,21] and suggested that YCT is promising for describing the intermediate-pressure regime [22,23]. The elevated-pressure regime was first elucidated in Ref. [24], where He, N_2, and CO_2 gas damping in long beam devices ($w \ll L$) confirmed YCT applicability at intermediate pressures (Kn ~ 1, Wi ~ 1) and explored the phenomenological model of vibrating spheres (MVS) for the high-pressure viscous regime (Kn $\ll 1$, Wi $\ll 1$). In this paper we offer a comprehensive evaluation of various theoretical models describing NEMSs in the fluidic environment. In the intermediate-pressure range, we find strong concerns about the SBT and demonstrate the superior performance of the YCT. However, in the high-pressure viscous regime, beyond the YCT applicability limits, the SBT shows good agreement with the experimental data and allows us to separately account for the damping and added mass, which makes the SBT more powerful comparing to the MVS. Extending the study to five gases (He, Ar, H_2, N_2, and CO_2), probing wider and shorter beams, and applying focused ion beam (FIB) milling to eliminate contributions from the undercut (an unavoidable defect of the standard fabrication technique), we clarify the physical meaning of the Yakhot viscosity μ_Y, establish the connection between μ_Y, the traditional viscosity μ, relaxation of molecular flow, and the number of degrees of freedom of the gas molecule, explore the SF contribution to the damping and spring constants of the device [25,26], and identify a correlation between the undercut and the effective radius in the MVS.

II. EXPERIMENT

The NEMS resonators, a series of cantilevers and bridges, were made by the top-down technique from standard silicon-on-insulator wafers. The SiO_2 mask was made by lift-off *e*-beam lithography; the Si was etched by continuous passivation in an inductively coupled plasma reactive ion etcher; the devices were released by etching the buried oxide layer using an isotropic buffered oxide etch. The parameters of the as-fabricated devices are summarized in Table I. Different width devices were placed on separate chips, so all devices on the same chip have the same width, 150, 250, 500, or 1000 nm. To facilitate capacitive electrostatic excitation of the resonator oscillations, their top surfaces were coated with a thin layer of aluminum ($d_{Al} \sim 30$ nm). Figure 1 shows a scanning electron microscopy (SEM) image of a typical as-manufactured device. The main source of the NEMS geometrical uncertainty is the undercut labeled u (Fig. 1), whose depth is slightly bigger than one-half of the device width: $u \approx 80$ nm for $w = 150$ nm, $u \approx 150$ nm for $w = 250$ nm, $u \approx 350$ nm for $w = 500$ nm, and $u \approx 700$ nm for $w = 1000$ nm. As will be clear from the further discussion, the undercut significantly reduces the precision of our experiment, except for the cases of long devices, $L \gg w$. The whole series of $w = 500$ nm devices was influenced by the undercut so strongly that the pressure

TABLE I. List of investigated samples.

No.	Type[a]	$w \times d_{Si} \times L$ (μm^3)[b]	t (μm)	f_0 (MHz)[c]
1	c	0.25 × 0.147 × 2.00	0.139	42.8
2	c	0.25 × 0.147 × 1.75	0.139	54.1
3	c	0.25 × 0.147 × 1.50	0.139	73.5
4	c	0.25 × 0.147 × 1.25	0.139	101.2
5	c	0.25 × 0.147 × 1.00	0.139	161.8
6	c^*	0.25 × 0.147 × 0.75	0.139	256.8
7	b	0.25 × 0.147 × 3.00	0.139	106.1
8	b	0.25 × 0.147 × 2.75	0.139	131.7
9	b^*	0.25 × 0.147 × 2.50	0.139	180.8
10	b^*	0.25 × 0.147 × 2.25	0.139	191.0
11	b^*	0.25 × 0.147 × 2.00	0.139	245.3
12	c	0.15 × 0.147 × 2.00	0.139	41.4
13	c	0.15 × 0.147 × 1.80	0.139	51.2
14	c	0.15 × 0.147 × 1.60	0.139	64.3
15	c	0.15 × 0.147 × 1.40	0.139	82.2
16	c	0.15 × 0.147 × 1.20	0.139	112.8
17	c	0.15 × 0.147 × 1.00	0.139	157.6
18	c	0.15 × 0.147 × 0.90	0.139	191.1
19	b	0.15 × 0.147 × 5.00	0.139	41.0
20	b	0.15 × 0.147 × 4.00	0.139	62.4
21	b	0.15 × 0.147 × 3.00	0.139	116.9
22	b	0.15 × 0.147 × 2.00	0.139	248.5
23	b	0.15 × 0.147 × 1.80	0.139	304.2
24	b	0.15 × 0.147 × 1.60	0.139	378.4
25	b	1.00 × 0.188 × 12.0	0.372	11.5
26	$c^\dagger$	0.50 × 0.147 × 2.00	0.139	34.2
27	$c^\dagger$	0.50 × 0.147 × 1.75	0.139	41.6
28	$c^\dagger$	0.50 × 0.147 × 1.50	0.139	54.0
29	$c^\dagger$	0.50 × 0.147 × 1.25	0.139	76.6
30	$c^\dagger$	0.50 × 0.147 × 1.00	0.139	108.2
31	$c^\dagger$	0.50 × 0.147 × 0.75	0.139	159.5
32	$b^\dagger$	0.50 × 0.147 × 3.00	0.139	89.3
33	$b^\dagger$	0.50 × 0.147 × 2.75	0.139	101.4
34	$b^\dagger$	0.50 × 0.147 × 2.50	0.139	146.7
35	$b^\dagger$	0.50 × 0.147 × 2.25	0.139	140.7
36	$b^\dagger$	0.50 × 0.147 × 2.00	0.139	166.7
37	$b^\dagger$	0.50 × 0.147 × 1.75	0.139	203.1

[a]Cantilever (c) or bridge (b); * denotes devices whose properties are strongly modified by undercut; † denotes the FIB-corrected devices.
[b]Nominal sizes of as-made devices *before* FIB corrections.
[c]Vacuum values of frequencies.

behavior of these devices was impossible to describe by any of the known models. In an attempt to reduce the influence of the undercut, the devices from this series were corrected using focused ion beam milling by means of narrow cuts separating the device from the undercut (see below). Another source of experimental uncertainty comes from the Al layer. SEM imaging showed that the Al layer on the freshly made sample has a grainy structure which overhangs by ∼5–8 nm from the sides of the device. However, after several cycles of pressure application, the NEMS surface becomes smooth and the overhang disappears. To measure the device properties, the frequencies f and damping coefficients γ, we used a room temperature ultrafast stroboscopic optical interferometry of free ring down oscillations excited by short electric pulses, applied between the substrate and the aluminum layer at the

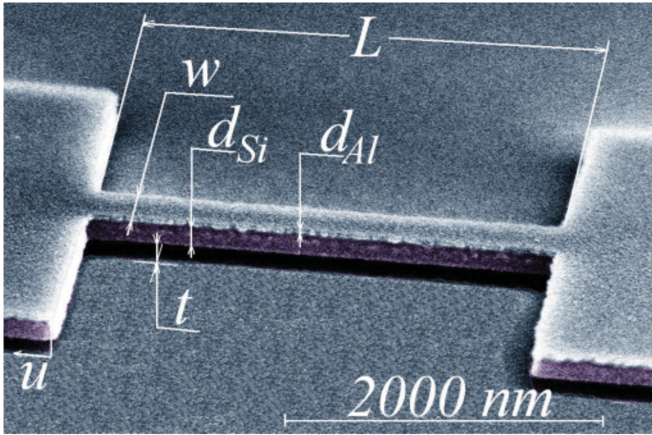

FIG. 1. (Color online) Scanning electron microscopy image of a typical device (bridge no. 8, Table I), taken before application of high pressure.

top of the device. A detailed description of this measurement technique is given elsewhere [27].

Figure 2 shows the typical oscillatory response of a NEMS resonator to an excitation pulse arriving at time $T = 0$. The amplitude of oscillations can be well approximated with the damped harmonic oscillator expression $A = A_0 e^{-\gamma T/2} \sin(2\pi f T + \phi)$, where A_0 and ϕ are the maximum amplitude and the initial phase. The inset in Fig. 2 demonstrates the high quality of the fabricated devices. As expected [28], the frequencies f_0 of the long ($L \gg w$) devices with the same thickness, measured in vacuum right after manufacturing, were proportional to $1/L^2$. Assuming that due to the grainy structure the density of the deposited Al layer constitutes 85% of the table density of the bulk material [29],

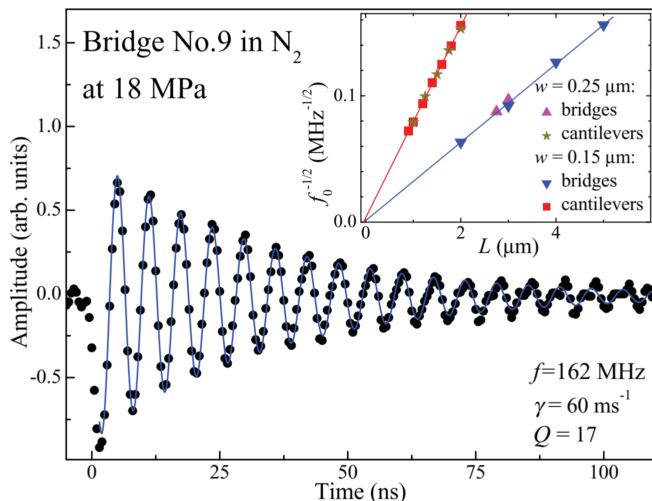

FIG. 2. (Color online) Real time free ring down of a typical gas-damped device (bridge no. 9, Table I) at 18 MPa after an excitation pulse arriving at time $T = 0$; the circles show measured data, the solid line represents a damped harmonic oscillator fit to experiment. The inset shows the square root of the vacuum values of the measured inverse fundamental resonance frequencies as a function of length for series of cantilevers and bridges; the straight lines are least-squares fits to the data.

and that the Young's modulus of the deposited Al layer is negligible in comparison to that of Si, the value of the Young's modulus of Si, estimated from the linear fit slopes [27], is $\sim$160 $\pm$ 10 GPa, in close agreement with the table value of 169 GPa for the $\langle 110 \rangle$ symmetry axis of silicon [30], which confirms the good precision of the nanofabrication process.

The pressure measurements were performed at room temperature using a specially designed optical chamber with sapphire window, as described in Ref. [31]. For the pressures of up to $\sim$2 MPa, a 2 mm thick window was used. For the higher pressures we used a 6 mm window. Because the thicker window introduces stronger optical distortions, the higher-pressure data have worse signal-to-noise ratio than the lower-pressure ones. This is especially noticeable on the short devices with high resonant frequencies. In order to avoid ruining the nanodevices by meniscus forces that appear during the CO_2 liquefaction, the CO_2 gas-liquid phase boundary was passed around the critical point. Although cycling through the high pressures did introduce changes in the Al layer of the devices, the main device properties were well reproducible, e.g., the overall shift of vacuum frequency after multiple cycling through the high pressure was about $\sim$0.5%.

III. RESULTS AND DISCUSSION

A. Road map for the data and analysis

The as-measured pressure dependences of the quality (Q) factor are demonstrated in Fig. 3 on the example of the bridges that have the same width $w = 250$ nm and thickness $d_{\mathrm{Si}} = 147$ nm, but different lengths L, as listed in lines 7–11 of Table I. The inset in Fig. 3(a) shows a classical sketch of the expected operating regimes [14]. At very low pressure (P), when there are only few gas molecules, the device Q factor is solely determined by its intrinsic value $Q_{\mathrm{intrinsic}}$ and does not depend on pressure. As the number of gas molecules increases with pressure, while Kn $\gg$ 1 (Wi $\gg$ 1), their interaction with the device is described by the FMF approximation [14] and

$$1/Q = 1/Q_{\mathrm{intrinsic}} + 1/Q_{\mathrm{FMF}}, \quad Q_{\mathrm{FMF}} = \omega m/(2\rho_f U w L), \tag{1}$$

where ρ_g is the gas mass density, and U is the root mean square velocity of the gas molecules. The range of applicability of the FMF approach is illustrated in Fig. 4 with solid lines on the example of two NEMS devices with $w = 500$ nm, (a) cantilever and (b) bridge (devices no. 27 and no. 33 from Table I, respectively). When the gas pressure is high, such that Kn $\ll$ 1 (Wi $\ll$ 1), the device properties are determined by its interaction with the viscous Newtonian fluid, so the classical expectation [14] is $Q \sim P^{-1/2}$. It is the crossover pressure range from FMF to viscous that we and others have focused on trying to better understand, through modeling and experiment, and it represents the inspiration for this article.

Solid and dotted lines, with slopes of -1 and $-1/2$, respectively, have been placed in each panel in Fig. 3. The first item of note is that, generally, the data do not follow either slope for most of the pressure range. In fact, the data trends are generally shallower in both regions, although there is usually a kink between a steeper region at the left and a shallower on the right. This implies that, not only is it the crossover regime

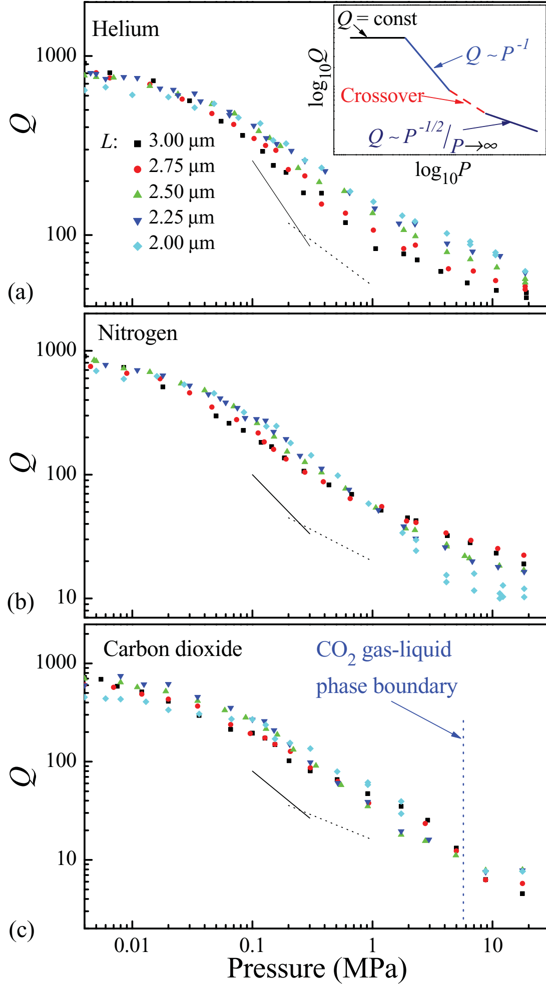

FIG. 3. (Color online) Measured values of the Q factor for bridges nos. 7–11 (Table I) in three gases: (a) helium, (b) nitrogen, and (c) carbon dioxide. The inset in (a) shows the expected schematic [14] of different damping regimes. The solid and dashed lines are to show the slopes for $Q \sim P^{-1}$ and $Q \sim P^{-1/2}$, respectively.

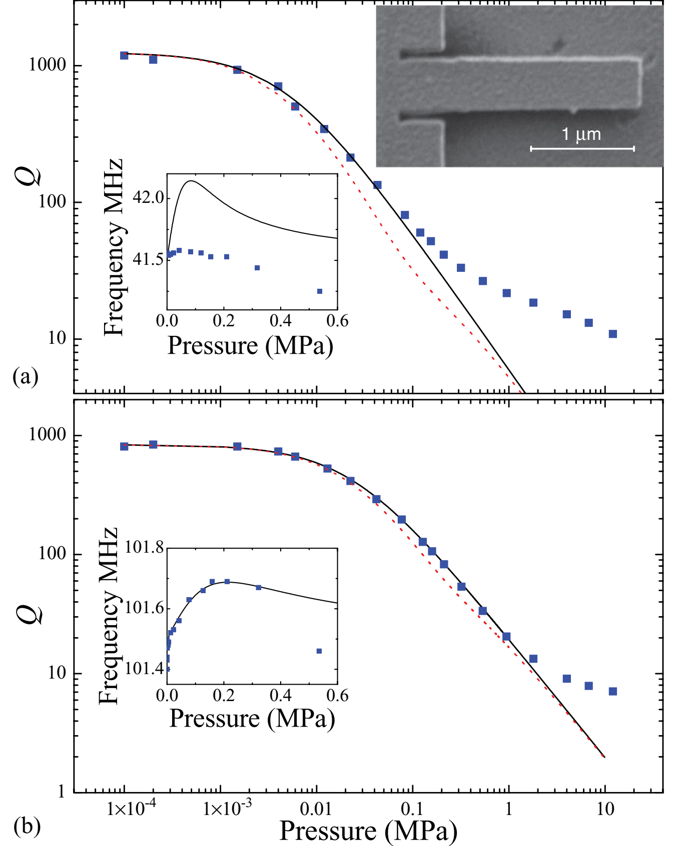

FIG. 4. (Color online) Pressure dependences of (a) cantilever no. 27 and (b) bridge no. 33 (Table I) Q factors in helium (solid squares). The solid lines show calculations using FMF [Eq. (1)]; the dotted lines show calculations using FMF corrected for the squeeze film Eqs. (3) and (4). The left insets show the pressure dependences of the measured frequencies (solid squares) and calculated frequency changes due to the SF added spring constants (solid lines). The right inset in (a) shows a SEM image of the device with FIB cuts separating it from the undercut shelf.

that is of interest, but much of the pressure range, in many of the devices, is not adequately explained by the canonical picture. There are also differences between the behavior in the different gases as well as between device lengths within a single gas. In He, the data enter the viscous regime at an earlier pressure, which is reasonable for a light but viscous gas. In the N_2 case, there is a change in behavior (the slope sharpens) as the devices shrink. Something clearly changes in going from 3 μm to 2 μm length in N_2. Is this a length scale crossing (cf. Kn $\sim$1) or a characteristic frequency crossing (cf. Wi $\sim$1) or an artifact of the device undercut and/or squeeze film effects?

These are the questions we hope to answer by applying various models in the various different pressure ranges. The main conclusion of these efforts is summarized at the end of the paper (Fig. 11) by overlaying the most successful models in their most successful regimes onto the Fig. 3 data. We also make efforts to shed light on the roles of squeeze film damping and the device undercuts in two ways: (i) by varying the device widths and (ii) by modifying the undercut by cutting the flaps on the sides of the devices using a focused ion beam as shown in the inset to Fig. 4.

B. Influence of squeeze film (low pressure)

To gauge the influence of the squeeze film without complications due to the undercut, we analyzed the damping behavior in the “undercut-free” FIB-modified devices with the results shown in Fig. 4. All our devices are fabricated from standard silicon-on-insulator wafers, such that the height of the device above the substrate, t (see Fig. 1 and Table I), is comparable to the device width w. This geometrical feature leads to the appearance of additional damping and spring forces due to the pumping action of the fluid effectively trapped in the space between the device and the substrate. For the case of rectangular-shaped beams, the squeeze film theory has been developed for the viscous regime only [25,32], predicting the value of the squeeze film damping in the viscous regime as

$$\gamma^v_{\rm sq} = \mu w^2/(t^3 \rho_b d_{\rm Si}), \qquad (2)$$

where μ is the fluid viscosity, and ρ_b is the density of the beam. However, for the analysis at low- and intermediate-pressure ranges the pressure dependence of the SF is needed.

Another approach to the SF was developed by Blech in the model for a parallel motion of oscillating rectangular plates [25,26]. This model predicts the squeeze film damping b_a and spring k_a forces as

$$b_a = \frac{64\sigma PwL}{\pi^6 \omega t} \sum_{i,j\ \mathrm{odd}} \frac{i^2 + \left(\frac{j}{\beta}\right)^2}{(ij)^2\left\{\left[i^2 + \left(\frac{j}{\beta}\right)^2\right]^2 + \frac{\sigma^2}{\pi^4}\right\}}, \quad (3)$$

$$k_a = \frac{64\sigma^2 PwL}{\pi^8 t} \sum_{i,j\ \mathrm{odd}} \frac{1}{(ij)^2\left\{\left[i^2 + \left(\frac{j}{\beta}\right)^2\right]^2 + \frac{\sigma^2}{\pi^4}\right\}}, \quad (4)$$

where the squeeze number $\sigma = 12\mu w^2\omega/Pt^2$, and $\beta = L/w$. In the high-pressure viscous regime, the damping force calculated from Eq. (3) becomes pressure independent and has the same value as that of Eq. (2). Later we will show that accounting for the SF damping in the viscous regime leads to significant improvement of the modeling results. However, using the SF model Eqs. (3) and (4) for the low- and intermediate-pressure regimes is problematic.

Figure 4 compares the measured Q factors of (a) cantilever no. 27 and (b) bridge no. 33 (Table I) with those calculated in the approximation of the pure FMF [Eq. (1)] regime (solid lines) and of the FMF regime corrected for the squeeze film Eqs. (3) and (4) effects (dotted lines). The FIB cutting (see right inset) of these devices ensures that the analysis is not complicated by the undercut since they effectively have none. Here, the unmodified FMF fares well in describing the damping at lower pressures. Note that the departure of the data from FMF behavior is later for the doubly clamped beam than for the cantilever of a similar geometry. This is the first hint that a Weissenberg picture may be more successful in describing the departure point than a Knudsen one. If the Knudsen number was the determining factor in the departure from FMF, the cantilever and the doubly clamped beam should deviate at the same pressure since they present the same cross section to the molecular flow. If the Weissenberg number is the determining factor, the higher-frequency device should deviate at a higher pressure, which is the case observed in Fig. 4.

The left insets compare the measured frequencies of the same devices with those predicted by Eq. (4). It is seen that in the case of a cantilever [Fig. 4(a)] an attempt to account for squeeze film effects significantly increases the mismatch between the measured and calculated values of the Q factor; the Blech theory also dramatically overestimates the squeeze film addition to the frequency of the cantilever. In the case of a bridge [Fig. 4(b)], similarly, the squeeze film correction of the Q factor worsens the agreement between the experimental data and theoretical curve, although the mismatch is not as big as in the case of the cantilever and the prediction of the bridge frequency increase due to the SF [Eq. (4)] is rather good up until at higher pressures the SF spring constant addition becomes negligible in comparison to the corrections due to the growth of the damping coefficient and the added mass load, which cause rapid decrease of the frequency.

From these observations we conclude that at the low pressures the Blech theory [25,26] is not suitable either for cantilevers or for bridges, although the discrepancy for bridges is smaller than that for cantilevers. An attempt to combine this SF theory [25,26] with calculations by Yakhot-Colosqui theory for low and intermediate pressure also leads to a similar conclusion. The inadequacy of the SF for reasonable fitting at low and intermediate pressures required us to neglect the effect in the modeling fits in these regimes. However, we believe that not accounting for SF effects may qualitatively explain some of the fitting deviations in the YCT modeling done in the next section.

C. Intermediate-pressure regime (Kn ∼ 1, Wi ∼ 1)

As we mentioned above, there are two alternative approaches to the intermediate pressure regime: SBT [15,16] and YCT [17,22,23].

1. Sader-Bhiladvala theory

Solving the Boltzmann equation, SBT for the damping force at the intermediate pressure (Kn $\sim$ 1) proposes [16]

$$\begin{aligned} b_{Bi} &= \rho_f U L w \pi^{3/2}\mathrm{Kn}/\alpha_b, \\ \alpha_b &= \ln(2\sqrt{\pi}\mathrm{Kn}/\mathrm{Ma}) - \gamma_e + 0.5 + \Lambda\sqrt{\pi}\mathrm{Kn}, \\ \Lambda &= 1 + 0.5(1 - e^{-\mathrm{Kn}/2}), \end{aligned} \quad (5)$$

where $U = \sqrt{3R\Theta/m_f}$ is the root mean square velocity of the fluid molecule, R is the universal gas constant, m_f is the molar mass of the fluid, Θ is the temperature, Ma is the Mach number, and $\gamma_e \approx 0.58$ is the Euler constant. Using this model gave only partially successful fits to the data and at the price of letting the characteristic device size be a fitting parameter with a value an order of magnitude or more smaller than expected.

The solid lines in Fig. 5 show attempts to use Eqs. (5) for fitting the damping of the bridge no. 7 at the intermediate pressures in three gases (a) He, (b) N_2, and (c) CO_2. One can see that in all cases the solid curves deviate strongly from the experimental data. In Ref. [22] it was suggested that such a deviation might be occurring due to the poor definition of the Knudsen number, used in Eqs. (5). Indeed, if we redefine the Knudsen number as $\mathrm{Kn} = \lambda_{\mathrm{mfp}}/w_K$, allowing the w_K to be a fitting parameter, we can have decent fits to the experimental data when $w_K = w/[30(\pm 5)]$, as shown with dotted lines in Fig. 5. For the broad $w = 500$ nm devices this correction is even bigger, up to 100 times; however, in this case we have an additional uncertainty due to inability to account for squeeze film effects. Although it is still possible that the mistake in Eqs. (5) could be fixable by a proper consideration of geometrical scaling factors, we conclude that the SBT approach to the intermediate pressure range presented in Ref. [16] requires revision.

2. Yakhot and Colosqui theory

Alternatively, the YCT [17,22,23] describes the fluid in terms of the Weissenberg number $\mathrm{Wi} = \omega\tau$, where the fluid relaxation time is assumed to be $\tau = \mu_Y/P$, and μ_Y is the Yakhot viscosity, a gas-specific constant with dimensions of viscosity [17]. The normalized damping $\gamma_n = \gamma m/S$, where m is the mass of the device, S is its surface area, and C_Y is a

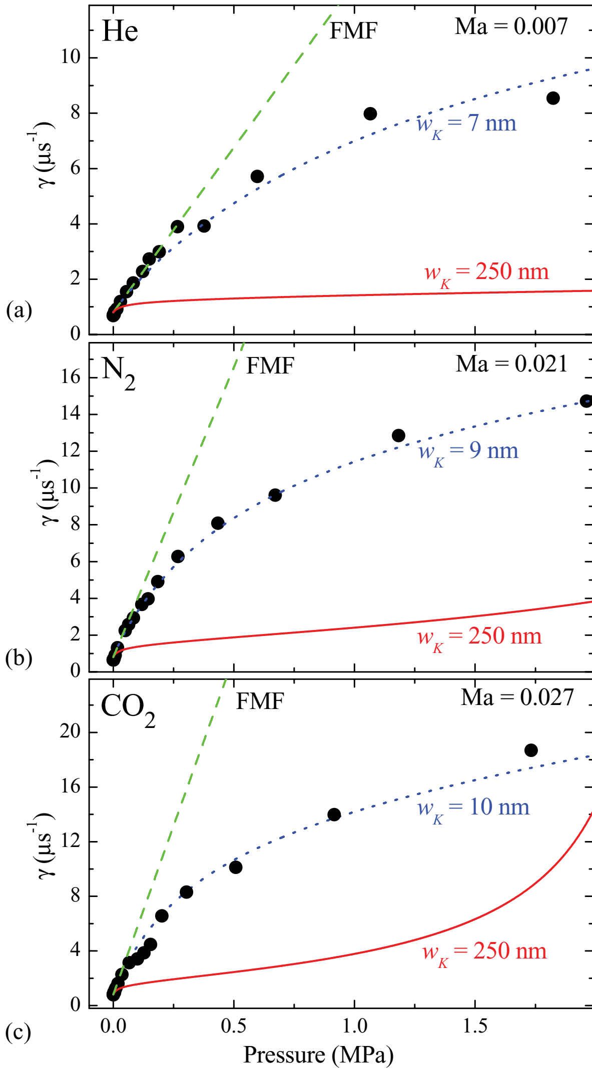

FIG. 5. (Color online) Attempt to use Bhiladvala's theory to fit damping in the intermediate pressure range (bridge no. 7, Table I) in (a) He, (b) N_2, and (c) CO_2. The figure demonstrates that obtaining a good fit would require a more than 25 times smaller characteristic size w_K used in the Knudsen number definition.

geometric corrective factor, is given by

$$\gamma_n = \frac{C_Y}{(1+\omega^2\tau^2)^{3/4}}\sqrt{\frac{\omega\mu\rho_g}{2}}\left[(1+\omega\tau)\cos\left(\frac{\tan^{-1}\omega\tau}{2}\right) - (1-\omega\tau)\sin\left(\frac{\tan^{-1}\omega\tau}{2}\right)\right]. \quad (6)$$

A preliminary analysis of the YCT approach [24] demonstrated that for the relatively long beams this model satisfactorily describes the low-pressure (high-$\omega\tau$) free molecular flow regime and the crossover occurring at $\omega\tau \sim 1$ up to $\omega\tau \sim 0.1$. In this work, testing the YCT on a bigger variety of the samples and gases, we give a more detailed exploration of the model.

Figure 6 shows a plot of γ_n as a function of pressure for selected devices of both long and short lengths in He, N_2, and CO_2 gases. Equation (6) is fitted to the data to pull out values for μ_Y and C_Y. The bump in the dissipation in each data set represents the moment when $\omega\tau \approx 1$ and defines the values

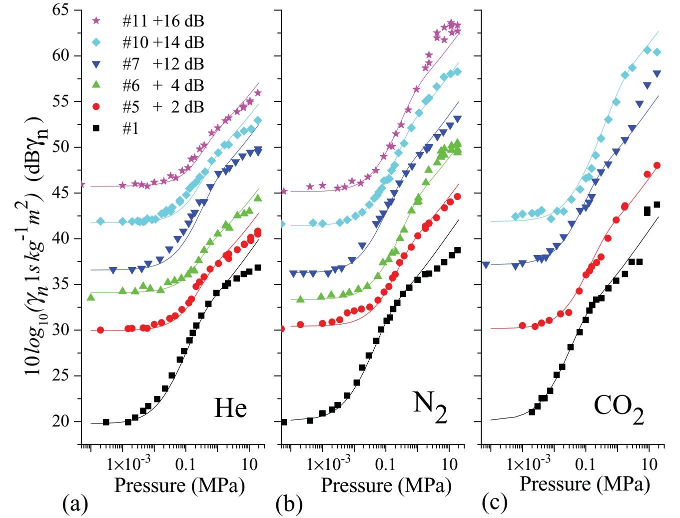

FIG. 6. (Color online) Examples of YCT fits Eq. (6) to the measured damping constant in (a) helium, (b) nitrogen, and (c) carbon dioxide for selected devices with $w = 250$ nm. For clarity, the neighboring curves are shifted with respect to their initial positions as marked.

for μ_Y. The fitting falls away at higher pressures as the viscous regime is entered, giving an idea for the range of applicability of YCT.

Table II shows the fit values for devices 1 through 25. For N_2, μ_Y stays at the same value of 0.6 ms Pa for the entire data set.[1] As μ_Y is supposed to be constant for a given gas, this is reassuring. However, in the case of He, μ_Y falls from 1.5 ms Pa for the longer devices to about 0.5 ms Pa for the shorter devices. The fits seen in Fig. 6(a) also deviate slightly at lower pressure. We expect that both effects are caused by not accounting for SF damping. Recall Fig. 4, where the SF effect results in increased dissipation at a given pressure in the crossover range. This additional damping pushes the data above the fit line here. Further, as the devices shrink and frequencies go up, there will be even more SF damping adding to the total. This additional damping can effectively shift the dissipation peak to the left for smaller devices (thus effectively causing a shift downward in μ_Y). The He should have substantially increased relative SF effects compared to N_2 because it is seven times lighter but with a similar value of viscosity. An alternative explanation for the changing μ value, that of the undercut becoming more important in shorter devices, should cause the N_2 to deviate as well, which is generally not the case. We will double-check this hypothesis shortly by going to different device widths as well as to FIB-modified devices. In the CO_2 gas, most of the devices can be fitted well with $\mu_{Y1}^{CO_2} = 0.4$ ms Pa and

[1]Although devices no. 6 and no. 11 appear to have a deviation at the high-pressure end in N_2, we do not alter the fit for these two cases. High-pressure N_2 was found to substantially suppress the optical readout signal in comparison to other compressed gases. This suppression, when combined with the smallest signal devices, made ring downs difficult to resolve and introduced large error into damping estimations (as evidenced by the scatter in these data).

TABLE II. YCT fitting parameters for the devices without FIB undercut correction (nos. 1–25 from Table I).

	$(\mu_Y \pm 30\%)^a$ (ms Pa)			$(C_Y \pm 30\%)^a$		
Device	He	N_2	CO_2	He	N_2	CO_2
1*c*	1.5	0.6	0.4	5.0	3.2	3.0
2*c*	1.5	0.6	0.4	4.6	3.0	2.6
3*c*	1.5	0.6	0.4	4.2	2.8	2.7
4*c*	1.0	0.6	0.4	3.6	2.7	2.5
5*c*	0.6	0.6	0.4	3.0	2.4	3.5
6*c*	0.4	0.6		2.5	3.2	
7*b*	1.5	0.6	0.4	3.5	2.4	2.5
8*b*	1.0	0.6	0.65	3.6	2.8	3.3
9*b*	0.8	0.6	1.5	3.0	3.0	6.0
10*b*	0.8	0.6	1.5	2.7	3.0	6.0
11*b*	0.5	0.6	1.5	2.7	3.4	6.0
12*c*	1.5	0.6		5.0	2.8	
13*c*	1.5	0.6		4.8	3.0	
14*c*	1.5	0.6		4.3	2.6	
15*c*	1.5	0.6		3.5	2.5	
16*c*	1.5	0.6		3.3	1.8	
17*c*	1.5*	0.6		3.4*	2.1	
18*c*	1.5*	0.6		3.4*	2.5	
19*b*	1.5	0.6		5.3	3.0	
20*b*	1.5	0.6		4.5	2.8	
21*b*	1.5	0.6		3.5	2.8	
22*b*	1.5*	0.6		2.8*	3.3	
23*b*	1.5*	0.6		3.3*	2.9	
24*b*	1.5*	0.6		3.3*	2.6	
25*b*		0.6			2.6	

[a]This is the maximum error as it is estimated for most of the shortest devices. For the long devices it is three times smaller. The label $*$ on a figure means that the error is $\sim$50%.

$C_{Y1}^{CO_2} = 2.2 \pm 0.5$; however, the higher-frequency devices again require different fitting parameters. We attribute this peculiarity to the precursor fluctuations occurring in the neighborhood of the CO_2 gas-liquid phase transition, discussion of which deserves a separate presentation.

A constant $\mu_Y^{N_2}$ versus a changing μ_Y^{He} turns out to explain the different behavior in Fig. 3. This can be seen after explicitly considering the crossover pressure P_X for each curve, that is, the pressure at which $\omega\tau \sim 1$. Since $\tau = \mu_Y/P$, $P_X = \mu_Y\omega$ at this crossover. Table III summarizes the crossover pressures for the selected devices.

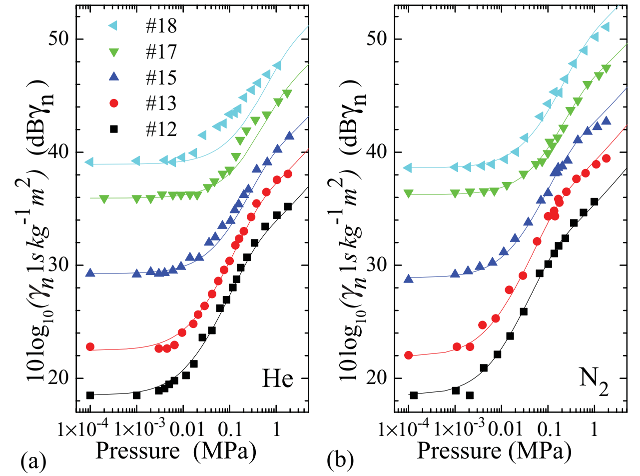

FIG. 7. (Color online) Examples of YCT fits Eq. (6) to the measured damping constant in (a) helium and (b) nitrogen for selected devices with $w = 150$ nm. For clarity, the curves are shifted with respect to each other by 3 dB.

Devices 7 to 11 are pertinent to Fig. 3. For He, these cluster to a similar value of P_X^{He} between 0.8 and 1.0 MPa. The decreasing μ_Y^{He} balances the increasing ω to give a single crossover pressure. This causes all data trends in Fig. 3(a) to look similar. For N_2, a constant $\mu_Y^{N_2}$ ensures that the crossover pressure grows from 0.4 to about 1 MPa. This is reflected in Fig. 3(b) with shorter devices crossing at higher pressures.

We now understand phenomenologically the difference in appearance between Figs. 3(a) and 3(b). We attempt to confirm the SF effect by checking the dissipation for narrower devices with $w = 150$ nm (nos. 12 through 24). The smaller width should decrease the SF effect relative to the overall damping. Indeed, the μ_Y^{He} value for He now stays constant at 1.5 ms Pa for the majority of the fits of the 0.15 μm wide devices. There is still a shifting to the left of the data compared to the fits at the short device lengths, as seen in Fig. 7(a) when the SF does finally become appreciable. The N_2 data, as before, always give $\mu_Y^{N_2}$ of 0.6 ms Pa and are fitted very nicely by the YCT [Fig. 7(b)]. The situation with the doubly clamped beam fits is similar.

To finally confirm that the SF is the dominant factor in the changing μ_Y, rather than undercut, we perform fits of the dissipation for the FIB-corrected devices with results shown in Table IV. These $w = 500$ nm wide devices should have strong SF effects in He gas, but zero undercut effects. Indeed,

TABLE III. Summary of the μ_Y (ms Pa) and crossover pressures P_X (MPa) for the selected devices.

Device	ω (s^{-9})	μ_Y^{He}	$\mu_Y^{N_2}$	$\mu_Y^{CO_2}$	P_X^{He}	$P_X^{N_2}$	$P_X^{CO_2}$	Figure
1	0.269	1.5	0.6	0.4	0.40	0.16	0.11	6
5	1.017	0.6	0.6	0.4	0.61	0.61	0.41	6
6	1.614	0.4	0.6		0.65	0.97		6
7	0.667	1.5	0.6	0.4	1.00	0.40	0.27	3, 6
8	0.827	1.0	0.6	0.65	0.83	0.50	0.54	3
9	1.136	0.8	0.6	1.5	0.91	0.68	1.70	3
10	1.200	0.8	0.6	1.5	0.96	0.72	1.80	3, 6
11	1.541	0.5	0.6	1.5	0.77	0.92	2.31	3, 6

TABLE IV. YCT fitting parameters for the devices where undercut was corrected with FIB (nos. 26–37 from Table I).

	$(\mu_Y \pm 30\%)$[a] ms Pa				$(C_Y \pm 30\%)$			
Device	He	Ar	H_2	CO_2	He	Ar	H_2	CO_2
26*c*	1.0	1.0	0.6	0.4	6.5	3.5	7.0	3.7
27*c*	1.5	1.0	0.6	0.4	6.5	3.4	7.0	3.5
28*c*	1.0	1.0	0.6	0.4	6.0	3.3	6.5	3.5
29*c*	0.8	1.0	0.6	1.0	5.5	3.3	6.0	4.4
30*c*	0.8	1.0	0.5	n/a	5.0	3.3	5.3	n/a
31*c*	0.5	3.0	0.5	n/a	5.0	4.5	5.0	n/a
32*b*	1.0	2.0	0.6	n/a	6.5	5.0	7.5	n/a
33*b*	1.0	2.5	0.6	n/a	6.5	5.2	7.0	n/a
34*b*	1.0	3.0	0.5	n/a	6.0	5.7	6.0	n/a
35*b*	1.0	4.0	0.5	n/a	5.5	7.0	6.5	n/a
36*b*	1.0	4.0	0.5	n/a	5.5	7.0	6.0	n/a
37*b*	1.0	n/a	0.5		4.5	n/a	5.5	

[a]This is the maximum error as it is estimated for the shortest devices. For the long devices it is three times smaller.

μ_Y is forced to change in the He gas (as well as in Ar gas) while it stays approximately constant in the low-viscosity (low-squeeze-film-effect) H_2 gas. The CO_2 fitting remains similar to the Table II case (the entry n/a for the higher-frequency devices in Table IV means that the intermediate regime is absent due to the closeness of the phase transition). The Yakhot viscosity for CO_2 exactly matches the previous value of $\sim$0.4 ms Pa; the corrective multiplier $C_{Y2}^{CO_2} = 3.5$ is somewhat higher, but this can be attributed to the SF effects. Figure 8 shows fits for devices no. 26 and no. 29 in these four gases.

The additional gases monitored in the FIB-cut devices also give further evidence for the intriguing notion that the Yakhot viscosity might be related to the molecular degree of freedom. The value of $\mu_Y^{H_2}$ for diatomic H_2 of 0.6 ms Pa (ignoring the slight decrease later in Table IV as coming from the SF) is identical to the $\mu_Y^{N_2}$ for diatomic N_2. Similarly, the noble gas argon has a μ_Y^{Ar} of about 1.0 ms Pa, which is similar to that of the noble gas helium.

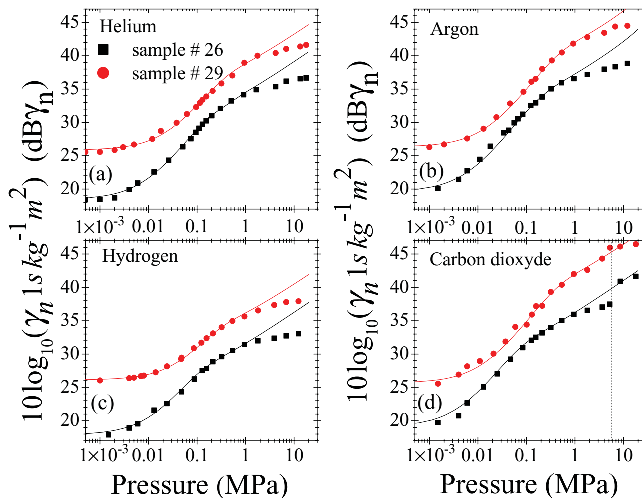

FIG. 8. (Color online) Examples of YCT fits Eq. (6) to the measured damping constant in (a) helium, (b) argon, (c) hydrogen, and (d) carbon dioxide for devices no. 26 and no. 29 with $w = 500$ nm. For clarity, the curves are shifted with respect to each other by 3 dB.

3. The meaning of μ_Y

Now we explore the meaning of μ_Y. Assume that the fluid relaxation time $\tau = \mu_Y/P$ is proportional to τ_c, such that $\tau = \alpha\tau_c$, where the proportionality constant α has the meaning of the number of molecular collisions necessary for thermalization of its motion. From kinetic theory, the gas viscosity μ is also nominally related to the molecular collision time τ_c as $\tau_c = 0.8\mu/P$. The Yakhot viscosity is thus directly connected to the traditional viscosity in the gas as

$$\mu_Y = 0.8\alpha\mu. \tag{7}$$

Using this relationship, we determine values for the collision number α for the various gases as summarized in Table V. Also shown are the values for α as calculated directly from τ_c using

$$\mu_Y = \alpha k_B\sqrt{\Theta M}/(4D^2\sqrt{\pi R_g}), \tag{8}$$

where M and D are the mass and diameter of the gas molecule, and k_B and R_g are the Boltzmann and universal gas constants. As concluded in Ref. [24] the values for α are generally considerably higher than expected for simple thermalization. This effect is not unexpected, because in the neighborhood of the vibrating beam the motion of the gas molecules is not independent, but correlated. The vibrating beam interacts with the large ensemble of the gas molecules and transmits momentum to all of them. Consequently, in order to thermalize its motion, a molecule needs to leave this correlated ensemble, which takes a large number of collisions. Also, this agrees with the trend noticed earlier [24] for gases with more internal

TABLE V. Summary of viscosity, Yakhot viscosity, and collision numbers in all five gases.

Gas	μ (μs Pa)	μ_Y (ms Pa)	α [Eq. (7)]	α [Eq. (8)]
He	20	1.5	94	117
H_2	9	0.55	76	97
Ar	27	1.0	46	50
N_2	19	0.6	39	42
CO_2	16	0.4	31	33

degrees of freedom to have a smaller collision number, with the exception of Ar. This trend is consistent with a correlated motion picture when considering the energy spread out among the molecular degrees of freedom; the higher degree of freedom gases could be expected to convert a smaller portion of their energy of collision with the vibrating beam into the correlated translational direction.

D. High-pressure viscous regime (Kn ≪ 1, Wi ≪ 1)

1. Squeeze film damping

As we mentioned above, in the high-pressure viscous regime (Kn ≪ 1, Wi ≪ 1) both approaches to the squeeze film damping [25,32], Eqs. (2) and (3), give similar values for this type of damping, which at high pressure is just a pressure-independent addition to the viscous damping. In He and N_2, where viscosity $\mu \approx 20\ \mu$Pa s, for the devices with $t = 139$ nm (devices nos. 1–24 and nos. 26–37 in Table I) the high-pressure values for squeeze film damping γ_{sq} are $\sim 0.5\ \mu s^{-1}$ for the devices with $w = 150$ nm; $\sim 1.3\ \mu s^{-1}$ for the devices with $w = 250$ nm; $\sim 5\ \mu s^{-1}$ for the devices with $w = 500$ nm. In gaseous CO_2, where $\mu \approx 16\ \mu$Pa s, for the devices with $w = 250$ nm the SF damping is 1.0 μs^{-1} and for the devices with $w = 500$ nm the SF damping is $\sim 4.5\ \mu s^{-1}$. For the devices with $w = 500$ nm in H_2 ($\mu \approx 9\ \mu$Pa s) the SF damping is $\sim 2.2\ \mu s^{-1}$; in Ar, whose viscosity changes throughout our pressure range from $\mu \approx 20$ to $\mu \approx 30\ \mu$Pa s, the SF damping increases with pressure from ~ 5.5 to $\sim 7.5\ \mu s^{-1}$. For the bridge with $w = 1\ \mu m$ in a nitrogen atmosphere (device no. 25 in Table I) with $t \approx 372$ nm the SF damping is $\sim 0.75\ \mu s^{-1}$. At the high pressures, accounting for SF damping leads to noticeable improvement of the quality of the theoretical fits to the measured data, so the rest of the discussion of the viscous regime concerns results after the SF damping effects are taken into account, unless the opposite is stated.

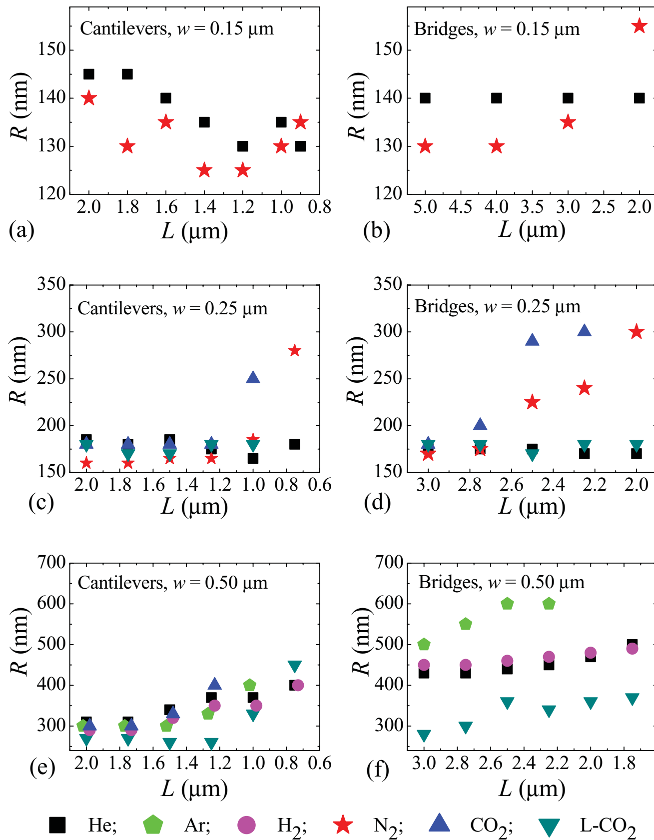

FIG. 9. (Color online) MVS [Eq. (9)] effective radii R for all devices in different gases as a function of the device length: (a) cantilevers nos. 12–18, (b) bridges nos. 19–24, (c) cantilevers nos. 1–6, (d) bridges nos. 7–11, (e) cantilevers nos. 26–31, and (f) bridges nos. 32–37 (Table I).

2. Model of vibrating spheres

The earlier analyzed [24] high-pressure MVS [33] represents the NEMS beam as a series of spheres whose radius R is an adjustable parameter:

$$Q = \frac{m\omega}{6\pi\mu R + 1.5\pi R^2\sqrt{2\mu\rho_f\omega}}, \tag{9}$$

where m is the device mass, and μ and ρ_f are fluid viscosity and density. Figure 9 shows how the value of R changes with the beam length for all types of beams in all gases. The dotted line in Fig. 10 shows example of the MVS fit to the device Q factor. Let us analyze Fig. 9 starting from panels (a)–(d). One can see that for almost all $w = 150$ nm devices in Figs. 9(a) and 9(b), in both helium and nitrogen, the value of $R \approx 135 \pm 10$ nm; the exception is the shortest 2 μm long bridge, where in a nitrogen atmosphere $R \sim 160$ nm (stars in Fig. 9). For long $w = 250$ nm devices in Figs. 9(c) and 9(d), $R \approx 175 \pm 10$ nm, but the shorter $w = 250$ nm devices are characterized by increase in the values of R up to $R \approx 300$ nm or higher. This increase is especially significant in heavier gases, CO_2 (up triangles) and N_2 (stars); however, it is not observed in the liquid CO_2 (down triangles). The increase of R characteristic of shorter devices we relate to the presence of

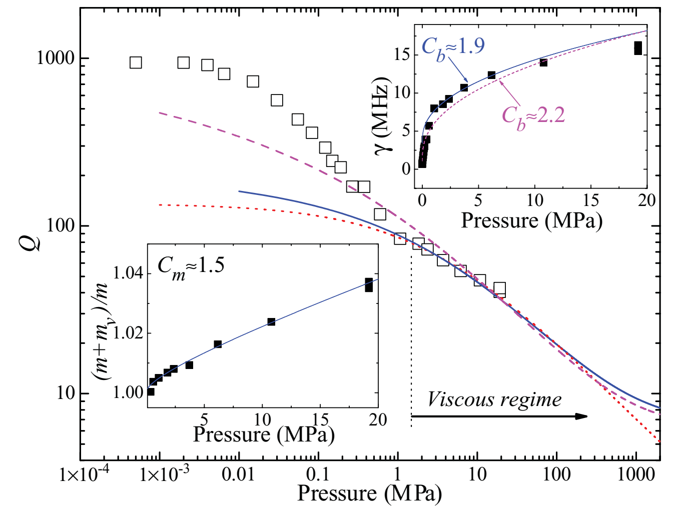

FIG. 10. (Color online) The pressure dependence of the bridge no. 7 (Table I) Q factor in helium, fitted with SBT [Eq. (11)] corrected for the SF (solid line), with pure SBT (dashed line), and with MVS (dotted line). The left inset shows the quality of the fit for the added mass, corrected by C_m. The right inset shows the fluid damping fitted with the SBT corrected for the SF (solid line) and with pure SBT (dashed line), multiplied by C_b.

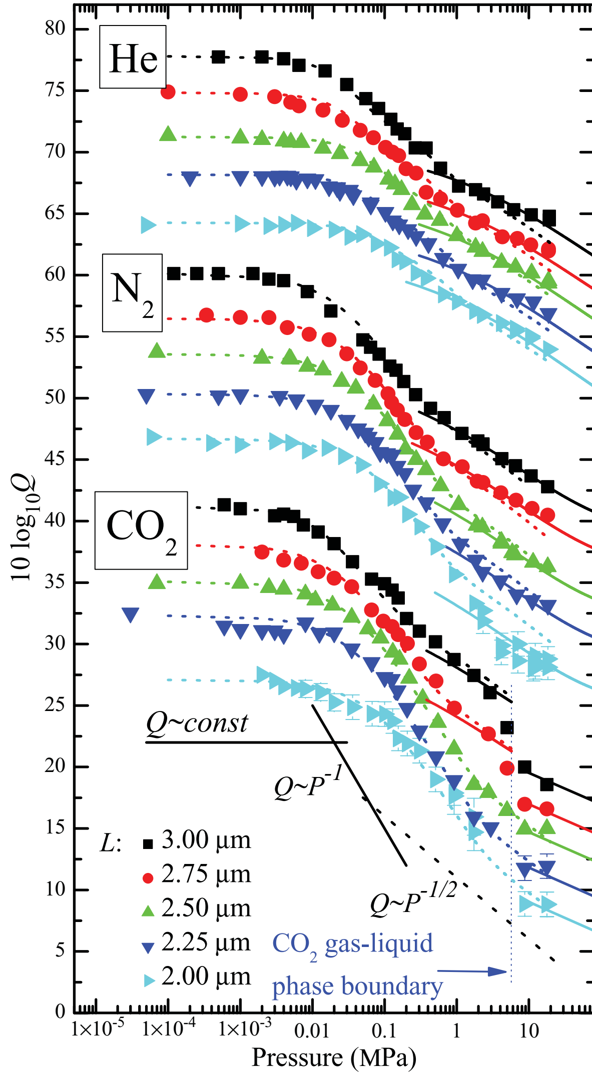

FIG. 11. (Color online) Q factors of bridges nos. 7–11 (Table I) as a function of pressure in three gases (symbols). The dotted lines show the fitting with YCT [Eq. (6)]; the solid lines are SBT fits Eq. (11). For clarity, the neighboring curves are offset by 3 dB; the offset of curves between the different gases is 6 dB. The measurement error bars are as shown or are of the order of the size of the symbols.

the undercut mentioned earlier, $u \sim w$ (Fig. 1). If the device length $L \gg u$, the undercut can be neglected. However, if the device is not sufficiently long, the presence of the undercut has to be accounted for. Otherwise, fitting the devices that have significant undercut using the simple MVS causes increase of the effective radius R. The higher the device frequency, the bigger is the influence of the undercut, and the bigger the value of R. In the overdamped conditions of liquid CO_2, however, the device frequencies are significantly reduced, so they can be approximated with the same values of R as for the longer devices [down triangles in Fig. 9(d)]. Thus, the ranges of stable values of R that are independent of L establish the applicability limits of the MVS. We marked the devices in which undercut cannot be neglected with asterisks in Table I.

In an attempt to reduce the influence of undercut, as we described earlier, we have applied a FIB correction to the $w = 500$ nm devices, as illustrated in the right inset in Fig. 4. As we mentioned above, before the FIB application the pressure behavior of these devices was impossible to describe by any of the theories. Figures 9(e) and 9(f) suggest that FIB application was fully successful only for devices with relatively low resonant frequencies, i.e., only for the three longest cantilevers with $R \approx 300 \pm 30$ nm in all gases [Fig. 9(e)]. Further decrease of the device length in all fluids, except for the overdamped conditions of liquid CO_2 where the device frequencies are reduced, requires significantly higher values of R, suggesting that such a thin cut as we made in the pressurized gas environment cannot fully insulate the vibrating device from the shelf because of the feedback through the fluid which is trapped inside the cut.

In the earlier report [24] we mentioned that for a $w = 1$ μm bridge (device no. 25 in Table I) the MVS effective radius is $R \approx 620 \pm 50$ nm. Of all four investigated widths considering only the long devices with negligible undercut, and assuming that for a zero-width device the parameter R should also be equal to zero, we can write for the width dependence of the MVS effective radius $R = 0.7(\pm 0.15)w$. A nice feature of the MVS theory is that it requires only one parameter with very transparent physical meaning.

3. *Sader and Bhiladvala theory*

An alternative to the MVS approach is offered by SBT [15,16], based on approximate solutions of the Boltzmann equations. With the assumption that rectangular-shaped NEMS beams can be substituted by cylinders, the damping force and the added mass can be written as

$$b_{Bv} = 0.25\pi\omega\rho_f L w^2 k_b \quad \text{and} \quad m_{Bv} = L w d_{\mathrm{Si}} \rho_f k_m, \qquad (10)$$

where k_b and k_m are coefficients expressed through the Bessel functions [16]. The strongpoint of this theory is that, provided geometrical factors are properly accounted for, it should be able to predict the values of the viscous damping and of the added mass separately. However, in order to obtain a quantitative agreement with the experimental data, we had to introduce scaling multipliers C_b and C_m:

$$b_v = C_b b_{Bv} \quad \text{and} \quad m_v = C_m m_{Bv}. \qquad (11)$$

The best values for the scaling multipliers C_b and C_m for all measurements performed on various devices in all gases are summarized in Tables VI and VII. It is seen that for all devices in all gases both scaling multipliers have values of the order of unity, especially if consideration is limited to the long devices, where there is no problem in accounting for the undercut. It is possible that these multipliers can be taken into account through more careful consideration of the geometry of the devices. Examples of fitting using Eqs. (10) and (11) are given in Fig. 10, where the left and right insets show the pressure dependences of the added mass and damping coefficients, respectively. The right inset in Fig. 10 also illustrates how the squeeze film damping addition improves the fit quality of the measured damping (compare solid and dashed lines). The quality of the fit for the Q factor fitting is illustrated in the main figure. It is seen that the solid curve in which the squeeze film damping is taken into account fits the data better than the dashed one, which ignores the squeeze film addition.

TABLE VI. SBT fitting parameters for the devices without FIB undercut correction (nos. 1–25 from Table I).

	$(C_b \pm 30\%)$[a]				$(C_m \pm 30\%)$[a]			
Device	He	N_2	CO_2	Liquid CO_2	He	N_2	CO_2	Liquid CO_2
1*c*	2.0	1.6	1.8	1.9	1.4	1.7	2.3	2.0
2*c*	2.0	1.6	1.8	1.7	1.4	1.5	2.3	2.0
3*c*	2.1	1.8	1.9	1.6	1.6	1.4	2.3	2.2
4*c*	2.1	1.7	2.1	2.0	1.4	1.6	2.6	2.1
5*c*	2.0	2.1	2.0	1.7	1.7	1.9	2.6	2.1
6*c*	2.4	5.0			1.4	4.0		
7*b*	1.9	1.8	2.4	2.2	1.9	1.9	2.6	2.5
8*b*	1.9	2.0	3.0	2.1	1.9	1.9	2.6	2.3
9*b*	2.0	3.1	n/a	2.3	1.9	2.1	n/a	2.6
10*b*	1.8	3.3	n/a	2.4	1.8	2.1	n/a	2.6
11*b*	2.1	5.0		2.8	1.8	2.6		3.0
12*c*	2.4	1.8			1.3	1.3		
13*c*	2.2	1.8			1.3	1.3		
14*c*	2.2	1.7			1.3	1.3		
15*c*	2.1	1.7			1.3	1.3		
16*c*	2.1	1.5			1.3	1.3		
17*c*	2.1	1.9			1.3	1.3		
18*c*	2.1	1.9			1.3	1.3		
19*b*	2.4	1.8			1.3	1.3		
20*b*	2.1	1.6			1.3	1.3		
21*b*	2.2	1.8			1.3	1.3		
22*b*	2.2	3.0			1.3	1.3		
23*b*	2.0	3.0			1.3	1.3		
24*b*	1.7	2.0			1.3	1.3		
25*b*		1.7				8.0		

[a]This is the maximum error as it is estimated for the shortest devices. For the long devices it is three times smaller.

For comparison, we also show the fitting with MVS (dotted line). In our pressure range the MVS and SBT curves closely follow each other. However, at the higher pressures, where for a Newtonian fluid the $P^{-1/2}$ behavior is expected, only the MVS curve follows this trend, while the SBT prediction significantly deviates from it.

IV. SUMMARY AND CONCLUSIONS

Figure 11 summarizes the models we considered in this work by demonstrating the quality of the fits to the experimentally measured Q factor values of the devices nos. 7–11 in all three gases (He, N_2, and CO_2) and in one liquid (CO_2). (i) In all cases, from vacuum throughout the free molecular and intermediate regimes up to the beginning of

TABLE VII. SBT fitting parameters for the devices where undercut was corrected with FIB (nos. 26–37 from Table I).

	$(C_b \pm 30\%)$					$(C_m \pm 30\%)$[a]				
Device	He	Ar	H_2	CO_2	Liquid CO_2	He	Ar	H_2	CO_2	Liquid CO_2
26*c*	1.7	1.5	1.7	2.2	1.0	3.2	3.7	2.8	6.0	3.7
27*c*	1.8	1.5	1.9	2.0	1.1	2.9	3.7	3.2	5.8	3.7
28*c*	2.2	1.8	2.2	2.4	1.3	3.3	3.7	2.9	5.8	3.6
29*c*	2.7	2.5	2.8	4.0	1.5	2.9	3.7	3.1	6.0	3.6
30*c*	2.4	3.3	2.8	n/a	2.8	2.9	3.7	3.1	n/a	3.7
31*c*	3.0	7.0	3.4	n/a	3.6	3.2	3.7	3.7	n/a	3.9
32*b*	3.4	4.2	3.7	n/a	2.4	3.7	5.2	4.3	n/a	5.0
33*b*	3.4	5.5	3.7	n/a	2.7	3.7	5.5	4.0	n/a	6.0
34*b*	3.4	8.5	3.7	n/a	4.0	3.7	8.0	3.8	n/a	6.0
35*b*	3.4	9.0	4.0	n/a	4.0	3.7	7.0	4.2	n/a	6.0
36*b*	3.9	20	4.4	n/a	4.0	3.7	15	4.2	n/a	6.0
37*b*	4.1	n/a	4.4		4.0	4.6	n/a	4.2		7.0

[a]This is the maximum error as it is estimated for the shortest devices. For the long devices it is three times smaller.

the high-pressure viscous regime, qualitatively good results can be achieved by using the Yakhot and Colosqui theory, neglecting the squeeze film effects (dotted lines). The value of the Yakhot viscosity is related to the fluid viscosity and to the number of molecular collisions necessary to thermalize the molecular motion, which, in turn, characterizes the degree of correlation of this motion. Also, μ_Y depends on the number of degrees of freedom of the participating gas molecules. (ii) In the high-pressure viscous regime, where $\omega\tau \lesssim 0.1$, nice fits can be obtained with the SBT model for the viscous flow with correction for the squeeze film damping effects (solid lines). A very strong point of this theory is that it distinguishes between the added viscous fluid mass and the viscous damping effects. (iii) Alternatively, at high pressure satisfactory results can also be achieved with a rather simple phenomenological model of vibrating spheres. Nevertheless, for quantitative agreement with the data, all these theories require scaling multipliers and/or fitting factors, whose values are summarized in Tables II–VII. In order to predict their numerical values, careful theoretical research devoted to exploration of the fluid properties and of the influence of the NEMS geometry is needed. The other important results of this work are as follows. (iv) Although the available theory for squeeze film effects, developed in the parallel rectangular plates approximation, can give a qualitative explanation of the observed effects, it apparently overestimates the squeeze film damping at low and intermediate pressures. Yet accounting for the squeeze film damping at high pressure improves the quality of the fits. This sets up the framework for the task of developing a low- and intermediate-pressure squeeze film model specifically for bridges and cantilevers. (v) The model suggested by SBT for the intermediate-pressure regime requires excessive scaling of the Knudsen number as a parameter. (vi) The suggested attempt to remove the influence of the undercut by FIB cutting with narrow (~30 nm) cuts was successful for relatively long devices only; apparently, high-frequency short devices need to have wider cuts separating them from the undercut shelf.

ACKNOWLEDGMENTS

This work was supported by NSERC, CIfAR, iCORE, CRC, and the National Institute for Nanotechnology (NINT). Samples were fabricated at the Nanofab of University of Alberta, and SEM imaging was performed at the NINT electron microscopy facility. N.L. was partially supported by an Avadh Bhatia Postdoctoral Fellowship. The authors are thankful to Professor Andriy Baumketner for fruitful discussion.

[1] A. K. Naik, M. S. Hanay, W. K. Hiebert, X. L. Feng, and M. L. Roukes, Nature Nanotechnol. **4**, 445 (2009).
[2] H. G. Craighead, Science **290**, 1532 (2000).
[3] M. Roukes, Sci. Am. **285**, 48 (2001).
[4] K. L. Ekinci, Y. T. Yang, and M. L. Roukes, J. Appl. Phys. **95**, 2682 (2004).
[5] Y. T. Yang, C. Callegari, X. L. Feng, K. L. Ekinci, and M. L. Roukes, Nano Lett. **6**, 583 (2006).
[6] C. T.-C. Nguyen, IEEE Trans. Ultrason. Ferroelectr. Freq. Control **54**, 251 (2007).
[7] A. Naik, O. Buu, M. D. LaHaye, A. D. Armour, A. A. Clerk, M. P. Blencowe, and K. C. Schwab, Nature (London) **443**, 193 (2006).
[8] M. Blencowe, Phys. Rep. **395**, 159 (2004).
[9] T. P. Burg, M. Godin, S. M. Knudsen, W. Shen, G. Carlson, J. S. Foster, K. Babcock, and S. R. Manalis, Nature (London) **446**, 1066 (2007).
[10] J. Dorignac, A. Kalinowski, S. Erramilli, and P. Mohanty, Phys. Rev. Lett. **96**, 186105 (2006).
[11] J. Arlett, Ph.D. Dissertation, California Institute of Technology, Pasadena, California, 2006.
[12] G. Y. Chen, T. Thundat, E. A. Wachter, and R. J. Warmack, J. Appl. Phys. **77**, 3618 (1995).
[13] Advanced Energy Consortium, Texas, USA, www.beg.utexas.edu/aec/.
[14] W. E. Newell, Science **161**, 1320 (1968).
[15] J. E. Sader, J. Appl. Phys. **84**, 64 (1998).
[16] R. B. Bhiladvala and Z. J. Wang, Phys. Rev. E **69**, 036307 (2004).
[17] V. Yakhot and C. Colosqui, J. Fluid Mech. **586**, 249 (2007).
[18] C. A. Van Eysden and J. E. Sader, J. Appl. Phys. **101**, 044908 (2007).
[19] R. A. Bidkar, R. C. Tung, A. A. Alexeenko, H. Sumali, and A. Raman, Appl. Phys. Lett. **94**, 163117 (2009).
[20] M. Li, H. X. Tang, and M. L. Roukes, Nature Nanotechnol. **2**, 114 (2007).
[21] S. S. Verbridge, R. Ilic, H. G. Craighead, and J. M. Parpia, Appl. Phys. Lett. **93**, 013101 (2008).
[22] D. M. Karabacak, V. Yakhot, and K. L. Ekinci, Phys. Rev. Lett. **98**, 254505 (2007).
[23] K. L. Ekinci, D. M. Karabacak, and V. Yakhot, Phys. Rev. Lett. **101**, 264501 (2008).
[24] O. Svitelskiy, V. Sauer, N. Liu, K.-M. Cheng, E. Finley, M. R. Freeman, and W. K. Hiebert, Phys. Rev. Lett. **103**, 244501 (2009).
[25] J. J. Blech, J. Lubr. Technol. **105**, 615 (1983)
[26] M. Andrews, I. Harris, and G. Turner, Sens. Actuators, A **36**, 79 (1993).
[27] N. Liu, F. Giesen, M. Belov, J. Losby, J. Moroz, A. E. Fraser, G. McKinnon, T. J. Clement, V. Sauer, W. K. Hiebert, and M. R. Freeman, Nature Nanotechnol. **3**, 715 (2008).
[28] A. N. Cleland, *Foundations of Nanomechanics. From Solid-State Theory to Device Applications* (Springer, Berlin, 2003).
[29] H. Du, J. Q. Xiao, Y. S. Zou, T. G. Wang, J. Gong, C. Sun, and L. S. Wen, Opt. Mater. **28**, 944 (2006).
[30] J. J. Wortman and R. A. Evans, J. Appl. Phys. **36**, 153 (1965).
[31] O. Svitelskiy, N. Liu, V. Sauer, K.-M. Cheng, E. Finley, M. Belov, M. R. Freeman, and W. K. Hiebert, Rev. Sci. Instrum. **79**, 093701 (2008).
[32] H. Hosaka, K. Itao, and S. Kuroda, Sens. Actuators, A **49**, 87 (1995).
[33] F. R. Blom, S. Bouwstra, M. Elwenspoek, and J. H. J. Fluitman, J. Vac. Sci. Technol. B **10**, 19 (1992); C. Lissandrello, V. Yakhot, and K. L. Ekinci, Phys. Rev. Lett. **108**, 084501 (2012).